Analysis of Low-Frequency Unsteadiness in the Direct Numerical Simulation of a Shockwave and Turbulent Boundary Layer Interaction

Stephan Priebe* and M. Pino Martin†

Department of Mechanical and Aerospace Engineering, Princeton University, Princeton, NJ 08544

The direct numerical simulation (DNS) of a compression ramp shockwave and turbulent boundary layer interaction (STBLI) is presented. The incoming flow conditions are Mach 2.9 and Re_θ 2900. The ramp angle is 24°. The dominant time scales in the flow are inferred from a spectral analysis of pressure signals along the wall, and pressure and massflux signals in the flow. The low-frequency shock motion in the DNS is broadband with a dominant frequency of approximately 900Hz, which is two orders of magnitude lower than the characteristic frequency of the turbulence in the incoming boundary layer. The present DNS is significantly longer in time than a previous DNS[1] and covers close to ten periods of the low-frequency unsteadiness (based on the dominant frequency). We also determine the statistical link between the shock motion and the fluctuations in the downstream, separated flow.

Nomenclature

δ	99% boundary layer thickness
δ^*	displacement thickness
ρ	density
θ	momentum thickness
C_f	skin-friction coefficient
f	filter function (or frequency)
i, j, k	computational coordinate in the streamwise, spanwise and wall-normal directions
L_{sep}	length of separated region
M	Mach number
p	pressure
Re_θ	Reynolds number based on the momentum thickness, θ
Re_{δ^*}	Reynolds number based on the displacement thickness, δ^*
T	temperature
u, v, w	streamwise, spanwise and wall-normal velocity
x, y, z	streamwise, spanwise and wall-normal coordinate

Subscripts

∞	freestream quantity
w	wall quantity

I. Introduction

It has been observed in many experimental studies of STBLI that the flow can be strongly unsteady, particularly when the shockwave is sufficiently strong to cause flow separation. Smits and Dussauge[2] show

*Graduate Student, AIAA Student Member.
†Assistant Professor, AIAA Senior Member.

that the shock motion may be decomposed into two parts, namely a spanwise wrinkling and a streamwise oscillation. The frequency of the spanwise wrinkling is comparable to the characteristic frequency of the turbulent motions in the incoming boundary layer, U_∞/δ, where δ is the 99% thickness of the incoming boundary layer and U_∞ is the freestream velocity. This must be contrasted with the streamwise oscillation which is at a much lower frequency, typically 1-2 orders of magnitude lower than U_∞/δ. It has been observed that the high-frequency spanwise wrinkling is caused by the structures in the incoming boundary layer, see e.g. the experiments by Erengil and Dolling,[3] Wu and Miles,[4] and the compression ramp DNS by Wu and Martin.[5] The cause of the low-frequency shock motion, however, is less clear. Recently, Ganapathisubramani et al.[6] proposed that elongated, low-momentum regions in the incoming boundary layer, so-called superstructures, might be driving the low-frequency shock motion. However, it has also been argued that the shock motion is caused by the downstream separated flow rather than the incoming boundary layer. From their DNS of a reflected STBLI, Pirozzoli and Grasso[7] proposed a mechanism whereby acoustic feedback in the separation bubble drives the shock motion. Dupont et al.,[8] and Dussauge et al.[9] reported evidence of a strong statistical link between the low-frequency shock motion and the downstream, separated flow.

Flows involving STBLI have been accessible to Large Eddy Simulations (LESs) and Direct Numerical Simulations (DNSs) for a number of years. Pirozzoli and Grasso[7] carried out a DNS of a reflected STBLI at Mach 2.25 and Re_θ 3725 for a deflection angle through the incident shock of 8.1°. They proposed the acoustic feedback mechanism mentioned above. Wu and Martin[1,5] performed the DNS of a 24° compression ramp at Mach 2.9 and Re_θ 2300. They validated their results (in terms of separation length, mean wall-pressure distribution, evolution of the mean flow through the interaction) against experiments by Bookey et al.[10,11] at matching conditions. In addition, Ringuette, Wu and Martin[12] validated the fluctuating wall-pressure in the DNS against the experiments by Ringuette and Smits.[13] The shock motion was inferred in the DNS from wall-pressure fluctuations, and mass-flux fluctuations in the freestream, and found to agree with a scaling previously proposed.[9] More recently, Touber and Sandham[14] performed the LES of a reflected STBLI at Mach 2.3 and Re_θ 5900, closely matching experimental flow conditions.[9] Various spanwise domain sizes were studied. One of their LESs was run for a long time and covers many periods of the low-frequency shock unsteadiness. A spectral analysis of wall-pressure signals shows a broadband peak at low frequencies around $S_L = f_s L_{sep}/U_\infty = 0.03$. Priebe, Wu and Martin[15] performed the DNS of a reflected shock STBLI at Mach 2.9 and Re_θ 2300 with a flow deflection through the incident shock of 12°. This simulation covers close to two periods of the low-frequency unsteadiness. The frequency of the unsteadiness was inferred from wall-pressure fluctuations near the separation point, and from pressure fluctuations in the freestream at the mean-shock location. It was found to agree with the scaling previously proposed.[9]

In the present paper, we perform the DNS of a compression ramp STBLI. The inviscid flow scenario for this configuration is shown in figure 1. The present DNS covers a significantly longer time than our previous DNS.[1] We perform a spectral analysis of pressure signals along the wall, pressure signals at the mean shock location in the flow, and massflux signals inside the separated flow region. We also determine the statistical link between the shock motion and the downstream separated flow, following a similar analysis as in previous experiments[8,9].

II. Computational Setup

II.A. General

We use the same general setup as that used by Wu and Martin[1] for the DNS of a 24° compression ramp flow at Mach 2.9 and $Re_\theta = 2300$.

The computational domain for the DNS, shown in Figure 2, measures approximately 8δ in the streamwise direction from the inlet to the corner and 6δ from the corner to the exit of the domain; in the spanwise direction, the domain measures 1.9δ; in the wall-normal direction, it measures approximately 4.5δ at the inlet. The grid for the DNS contains 1024×160×128 grid points in the streamwise, spanwise and wall-normal directions, respectively. It is apparent from Figure 3 that the grid is clustered both in the wall-normal direction near the wall and also in the streamwise direction near the corner.

The details for the numerical code are as follows: the inviscid fluxes are discretized in space using a 4th-order accurate weighted essentially nonoscillatory scheme (WENO), which is both linearly and non-linearly optimized.[16,17,1] For the spatial discretization of the viscous fluxes, 4th-order accurate central differencing is used, and time-integration is performed with a 3rd-order accurate, low-storage Runge-Kutta algorithm. The DNS code has been validated by Wu and Martin[1] against the experiments of Bookey, Wyckham and

Smits[11] at matching flow conditions.

At the wall, a no-slip, isothermal boundary condition is used. The prescribed wall temperature is 307K, which is close to the adiabatic wall temperature. At the top and outlet boundaries, a supersonic exit boundary condition is used. A significant difference between the present simulation and that of Wu and Martin[1] is the type of inlet boundary condition used. Wu and Martin[1] use a rescaling box at the inlet of the computational domain. In contrast, in the present simulation, the inlet boundary condition is prescribed from a separate boundary layer DNS (described below). This means that the rescaling is not performed as part of the compression ramp DNS. Instead, it is performed as part of the separate boundary layer DNS, the results of which are then used as an inflow boundary condition for the compression ramp DNS. Performing a separate boundary layer DNS to generate the inflow boundary condition has several advantages, including the possibility of reusing the boundary condition for other STBLI simulations.

II.B. Inflow Boundary Condition

As described above, the inflow boundary condition is supplied by a separate boundary layer DNS. The domain for that DNS measures approximately 9δ in the streamwise direction, 2δ in the spanwise direction and 9δ in the wall-normal direction. The grid for the DNS contains 410×160×112 grid points in the streamwise, spanwise and wall-normal directions, respectively. At the inlet of the computational domain, the rescaling boundary condition of Xu and Martin[18] is used. The recycling station is located approximately 8δ downstream of the inlet. It is also at this position that the flow is sampled at every timestep to provide the inlet boundary condition for the compression ramp DNS.

There is an important difference between the present boundary layer DNS and the simulations we have previously reported (such as e.g. Martin,[19] or Xu and Martin[18]). In the present simulation, the fluctuations in the freestream are damped, or filtered, approximately every $75\delta/U_\infty$. The filter only acts in the freestream; the boundary layer flow itself is left unchanged. The justification for using such a flow filter in the freestream is as follows: In order to investigate the low-frequency shock motion, the simulation must be run for a sufficiently long time to cover an appropriate number of periods of the unsteadiness. We have found that over such long runtimes, the level of fluctuations grows in the freestream. The growth rate is moderate (of the order of 1% in the level of pressure fluctuations over a time scale of the order of 100s of δ/U_∞), but over the very long runtimes required here the level of noise in the freestream becomes unacceptable. Since this noise accumulation is an unphysical artifact of the simulation, we damp the fluctuations in the freestream. This enables the DNS to be run for sufficiently long times to investigate the low-frequency unsteadiness.

The filtering is performed on the conservative variables, according to

$$u(x,y,z) = \overline{u(z)} + f(z)u'(x,y,z) \tag{1}$$

where u is the filtered variable, $\overline{u}$ is the streamwise-spanwise mean of the unfiltered variable, u' is the local fluctuation of the unfiltered variable, and f is the filter function. A value of $f = 0$ means that the fluctuations are completely damped out, whereas $f = 1$ means that the flow is left unchanged. The filter function is defined to depend only on the wall-normal coordinate, z (or, equivalently, the wall-normal computational coordinate, k). It varies according to a hyperbolic tangent function:

$$f(k) = \frac{1}{2}\left\{1 - tanh\left[c\frac{k-k_m}{k_e-k_s}\right]\right\} \tag{2}$$

where k_e and k_s are constants, k_m is defined according to $k_m = (k_e+k_s)/2$, and c is a constant. The values for the constants are: $c = 1.0$, k_e is the computational coordinate that corresponds to a wall-normal coordinate of $z = 1.6\delta$, and k_s is the computational coordinate that corresponds to a wall-normal coordinate of $z = 1.8\delta$. These constants are chosen such that the filter does not operate on the actual boundary layer and is only 'switched on' in the freestream above $z = 1.5\delta$, see figure 4. This ensures an accurate, physical simulation of the boundary layer while also fulfilling the goal of damping the noise in the freestream. Figure 5 plots the van Driest-transformed velocity profile for the DNS. The profile follows the log law accurately. Figure 6 plots the spanwise-averaged mass-flux signal in the freestream at $z = 1.6\delta$. Both the signal for the original, unfiltered DNS and for the filtered DNS are shown, illustrating that the filtering works to damp the undesired and unphysical growth of the fluctuations in the freestream.

	M	Re_θ	θ (mm)	δ^* (mm)	C_f	δ (mm)	ρ_∞ (kg/m^3)	U_∞ (m/s)	T_∞ (K)
Experiment[10,11]	2.9	2400	0.43	2.36	0.00225	6.7	0.074	604.5	108.1
DNS[1]	2.9	2300	0.38	1.80	0.00217	6.4	0.077	609.1	107.1
present DNS	2.9	2900	0.48	2.62	0.00219	7.3	0.076	609.8	108.9

Table 1. Conditions for the incoming turbulent boundary layer.

Figure 7 shows the streamwise velocity spectrum as a function of wavenumber in the log layer of the filtered boundary layer DNS. The spectrum consists of a broadband peak associated with the turbulent motions. Superimposed on this broadband peak are peaks associated with the rescaling frequency and with its second and higher harmonics. We note that the spectrum contains little energy at wavenumbers less than $k\delta = 0.4$. An important point to note from figure 7 is that the filtering does not introduce any significant forcing in the spectrum. This was confirmed for all heights across the boundary layer. Furthermore, the filtering does not introduce any noticeable forcing in the freestream (where the filter is 'switched on') as is apparent from the streamwise velocity spectrum at $z = 1.8\delta$, shown in figure 8. The rescaling peaks are seen to be dominant in the freestream with only very weak turbulence activity.

We thus conclude that the filtering produces an accurate, physical simulation over long runtimes without any noise accumulation in the freestream. There is no noticeable forcing at the filtering frequency, as we have demonstrated from the velocity spectra above.

III. General Characterization of the Flowfield

The flow conditions in the present compression ramp DNS are summarized in table 1. The table also includes the flow conditions for the previous DNS of Wu and Martin,[1] and the experiments against which it was validated.[10,11]

The flow conditions for the present DNS are similar, but not identical, to the previous simulation and experiments. In the present DNS, the boundary layer is thicker, and the Reynolds number is higher. These differences are entirely due to the longer development length in the present simulation. This longer development length results from the fact that the inflow boundary condition is provided by a separate boundary layer DNS.

Due to the difference in the flow conditions noted above, we observe a small difference in the location of the separation and reattachment points between the present DNS and that of Wu and Martin.[1] In the DNS of Wu and Martin,[1] the mean-flow separation point is located approximately 18.9mm upstream of the corner. In the present simulation, the separation points is about 16% closer to the corner, at 15.8mm. A similar difference is observed in the location of the mean-flow reattachment point, which is 8.2mm downstream of the corner in the DNS of Wu and Martin[1] and 6.9mm downstream of the corner in the present DNS. The separation length, L_{sep}, is thus reduced by 16% between the DNS of Wu and Martin[1] ($L_{sep} = 27.1$mm) and the present DNS ($L_{sep} = 22.7$mm). In non-dimensional terms, the separation point for the present DNS is located at $x = -2.2\delta$, and the reattachment point is located at $x = 0.9\delta$.

IV. Spectral Analysis of the Flowfield

At locations in the flowfield that are of particular interest, the flow variables are sampled at a frequency of 16.2MHz from the DNS (the sampling frequency corresponds to one sample for every 10 iterations in the simulation). In this section of the paper, we present the spectral analysis of these signals. We establish the dominant time scales in the flow as well as the statistical link between the motions in different regions of the interaction.

The locations in the flowfield that we consider are shown in figure 9. Figure 9(a) shows the general organization of the mean flow to help illustrate the location of the sampling points relative to the principal flow features. The shock wave is indicated by the contour line $|\nabla p| = 3.0 p_\infty/\delta$ in the figure; the underlying flood contour of u_{rms} highlights the shear layer, which originates near the separation point and bounds the

separation bubble; the mean-flow separation and reattachment points are also indicated in the figure. The companion figures 9(b)- 9(d) illustrate the location of the sampling points in the DNS.

There are five sampling points along the wall, as shown in figures 9(b). The point denoted 'W1' is located at $x = -2.4\delta$, which is near the the mean-flow separation point at $x = -2.2\delta$. Progressing downstream, the point denoted 'W2' ($x = -1.8\delta$) lies in the shock motion region and in the mean-flow separation bubble. The point 'W3' ($x = -1.5\delta$) also lies inside the mean-flow separation bubble, but downstream of the shock motion region. The point 'W4' is located at the corner ($x = 0.0\delta$), and the point 'W5' ($x = 1.0\delta$) is located near the mean-flow reattachment point. (There are also sampling points in the undisturbed incoming flow and in the downstream flow, but these are not shown here).

Figure 9(c) shows the location of the sampling points in the shear layer and separation bubble. The point denoted 'SL1' is located at the origin of the shear layer near the mean-flow separation point. It is the point where the value of u_{rms} assumes a maximum at this particular streamwise station. The second sampling point in the shear layer, 'SL2', is located above the corner and near the apex of the separation bubble. Again, it is the point of maximum u_{rms} at this particular streamwise station. The two remaining points shown in figure 9(c), 'SB1' and 'SB2', are located inside the separation bubble, above the corner. At the point 'SB1', the mean streamwise velocity is zero, and at the point 'SB2' the streamwise velocity has a minimum (i.e. the reversed velocity has a maximum, which equals about 4.3% of the freestream velocity).

The four sampling points shown in figure 9(d) ('MS1' through 'MS4') are all located at the mean shock location, but at different heights above the wall. 'MS1' is located at $z = 0.6\delta$ (and thus inside the boundary layer). The remaining points are outside the boundary layer: 'MS2' is located at $z = 1.3\delta$, 'MS3' at $z = 1.9\delta$ and 'MS4' at $z = 2.7\delta$. The mean shock location is determined using a pressure-threshold criterion. At fixed height above the wall, the location of the shock is identified with the first point encountered in a streamwise sweep of the computational domain (starting from the inlet), for which the pressure is greater than $1.27p_\infty$.

IV.A. Wall-pressure Signals and Spectra

The wall-pressure signals at different streamwise locations are shown in figure 10. The orange signal, which is obtained at $x = -2.4\delta$ near the mean-flow separation point, displays low-frequency oscillations. Such oscillations are also visible in the black signal, which is taken just downstream of the mean-flow separation point. The low-frequency oscillations in the wall-pressure can be attributed to the motion of the shock system over the sampling locations.

Figure 11 shows the spectra of some of the wall-pressure signals. The locations in the interaction region are referenced by the abbreviations 'W1' through 'W5', as introduced above (see also figure 9(b)). It is apparent from Figure 11(a) that the wall-pressure spectrum in the incoming, undisturbed boundary layer contains a broadband turbulence peak, centered around a frequency of 10^5Hz. The effect of the rescaling on the flow is also visible from this spectrum in the form of peaks occurring at the characteristic rescaling frequency of 10^4Hz and at the second and third harmonic of the rescaling frequency. These peaks are narrow and confined, and consequently they carry little energy. Furthermore, they are at least a decade away from the low-frequency range associated with the shock motion and hence do not pollute the range of frequencies that are of interest here. In fact, it is apparent from 11(a) that the wall-pressure fluctuations in the incoming boundary layer carry virtually no energy at frequencies below 10^4Hz. Figure 11(a) also shows the spectrum at point 'W1', near the mean-flow separation point. Compared to the upstream flow, this spectrum has less energy in the range of frequencies associated with the turbulence. A significant portion of the energy is contained at much lower frequencies associated with the shock motion. This energy is broadband and centered around a frequency of approximately 900Hz. Progressing further downstream into the separation bubble, the spectrum at location 'W3' still contains significant energy at the low frequencies around 900Hz, although the peak is less dominant than near the separation point at 'W1' (see figure 11(b)). We also note that the broadband peak associated with the turbulent motions is centered around a frequency of approximately 5×10^4Hz. In other words, the dominant turbulence frequency has shifted from a value of around 10^5Hz in the incoming boundary layer to a lower value of 5×10^4Hz in the separation bubble. The spectrum at location 'W5' (shown in figure 11(c)) is similar to that at 'W3', the only difference being a further reduction in the energy at the low frequencies to the point where little energy persists in the range of frequencies associated with the shock motion. Figure 11(d) shows the spectrum in the downstream flow at $x = 4.5\delta$. At this location, there is almost no energy at the low frequencies, and the spectrum consists of a broadband turbulence peak centered around a frequency of approximately 5×10^4Hz. We note that the characteristic frequency of the turbulence in the downstream flow, U_∞/δ, is also approximately 5×10^4Hz.

IV.B. Pressure Signals and Spectra at the Mean Shock Location in the Flow

Figure 12(a) shows the pressure signal at the location 'MS1', that is, at the mean shock location at a distance $z = 0.6\delta$ above the wall. The low-frequency oscillations caused by the motion of the shock system over the sampling point are apparent. For this point, which is located in the boundary layer, the low-frequency oscillations are relatively smooth. This must be contrasted with the pressure signals obtained at the mean shock location outside of the boundary layer, in the freestream, which display a more intermittent character. Figure 12(b), which shows the pressure signal at the location 'MS3' in the freestream, is an example of this intermittent behavior. (The pressure signals at the other two locations in the freestream, namely 'MS2' and 'MS4', are very similar to the one at 'MS3' and omitted here for brevity).

The power spectra of the pressure signals at the mean shock location are shown in figure 13. Both the signal at location 'MS1' (in the outer part of the boundary layer) and 'MS3' (in the freestream) carry most of their energy in a broadband peak at low frequency. The peak is centered around a frequency of approximately 900Hz, which agrees with the value observed from the wall-pressure signals in the vicinity of the mean-flow separation point. At higher frequencies, however, the spectrum at 'MS1' and 'MS3' show some differences. The energy peak at the rescaling frequency and at its second harmonic, while barely discernible at 'MS1', are more important at 'MS3'. This may be attributed to the fact that in the freestream the turbulence fluctuations are weaker than in the boundary layer, so that the relative importance of the rescaling forcing is greater in the freestream than in the boundary layer. That being said, we note that the rescaling peaks are relatively confined and narrow and do not carry a very large amount of energy. Furthermore, the rescaling frequency is approximately a decade greater than the characteristic shock motion frequency and hence does not pollute the range of low frequencies that are of interest here.

IV.C. Flow Scales Inside the Separated Flow Region

Figure 14(a) shows the spectra of streamwise massflux at two locations in the separated shear layer (one location, 'SL1', is just downstream of the mean-flow separation point, and the other, 'SL2', is near the apex of the separation bubble, above the corner). The spectra are similar, displaying a broadband peak, which is centered around a frequency of approximately 3.0×10^4Hz. This frequency is significantly lower than the characteristic turbulence frequency in the incoming boundary layer, which is approximately 10^5Hz. Furthermore, the spectra carry significant energy in the low frequency range of the shock motion.

Figure 14(b) shows the spectra of streamwise massflux at two locations inside the separation bubble (both locations are above the corner; one location, 'SB1', coincides with the point of zero streamwise velocity, and the other, 'SB2', coincides with the point of maximum reversed velocity). The spectra are similar, displaying a broadband peak, which spans the entire range of investigated frequencies. The broadband peak is centered around a frequency of approximately $7.0 \times 10^3 Hz$. There is a significant amount of energy at the low frequencies characteristic of the shock motion.

IV.D. Statistical Link between Shock Motion and Separated Flow

The magnitude-squared coherency function between two signals a and b is defined as

$$coh(f) = \frac{|P_{ab}(f)|^2}{P_{aa}(f)P_{bb}(f)} \tag{3}$$

where P_{aa} and P_{bb} are the power spectral densities of the signals a and b, respectively, and P_{ab} is the cross-power spectral density. The coherency function takes values between 0 and 1. It indicates, as a function of frequency, how well signal a corresponds to signal b. A value of 1 means that the signals are related as in a linear system.

Figure 15 shows the magnitude-squared coherency function between the wall-pressure signal near the mean-flow separation point (W1) and different points under the separation bubble, up to the mean-flow reattachment point. It is apparent from figure 15(a) that the wall-pressure fluctuations near the mean-flow separation point are strongly linked, at the low frequencies of the shock unsteadiness, with the wall-pressure fluctuations downstream of the shock motion region, in the separated flow region. The coherency reaches a maximum value of nearly 0.9. Peaks of moderate coherency also occur at the rescaling frequency and its second harmonic, as expected. Progressing further downstream, figure 15(b) shows that the wall-pressure fluctuations near the mean-flow separation point are strongly linked, at the low frequencies of the

shock unsteadiness, with the wall-pressure fluctuations at the corner, inside the separated flow region. The maximum coherency attained is approximately 0.65. However, the plot looks qualitatively different at low frequency than figure 15(a), in the sense that the coherency shows a distinct peak around a frequency of $10^3 Hz$. It does not continue to rise up to the lowest resolved frequency as it does in figure 15(a). Figure 15(c) shows the coherency between the wall-pressure fluctuations near the mean-flow separation point and those near the mean-flow reattachment point. It is qualitatively identical to figure 15(a) discussed above, except that the level of coherency is a bit lower. Nevertheless, a significant coherency at the low frequencies of the shock unsteadiness is still apparent. It thus appears that the fluctuations near the separation point are statistically coherent, at the low frequencies of the shock unsteadiness, with the fluctuations throughout the separation bubble, all the way up to the reattachment point.

We can extend this analysis to include the motion of the shock in the freestream. In figure 16, we compute the coherency between the pressure signal at the mean shock location in the freestream (location MS2) and the pressure signals at different points along the wall. All plots show a strong coherency at the low frequencies of interest. As expected, the coherency is strongest near the separation point (maxima around 0.9) and somewhat weaker, but still significant, close to the reattachment point. It thus appears that the motion of the shock in the freestream is statistically coherent, at the low frequencies of the shock motion, with the fluctuations near the separation point, inside the separated flow region and at the reattachment point.

These findings agree with the experimental findings of Dussauge, Dupont and Debiève,[9] and Dupont, Haddad and Debiève [8] for a reflected shock interaction at low Reynolds number.

Figure 17 shows the coherency between the pressure at the mean shock location in the freestream and the massflux at different points inside the separation bubble and separated shear layer. Again, all plots show significant coherency at the low frequencies of the shock unsteadiness, although the levels are lower than in figure 16 above.

V. Conclusions

The DNS of a 24° compression ramp STBLI at Mach 2.9 and Re_θ 2900 is presented. The shock motion frequency is inferred from wall-pressure signals near the separation point, and from pressure signals in the freestream at the mean shock location. The spectra show a broadband peak, centered around a frequency of approximately 900Hz, which is two orders of magnitude less than the characteristic frequency of the turbulence in the incoming boundary layer. The wall-pressure spectra under the separation bubble, as well as the massflux spectra inside the separation bubble and separated shear layer, show a shift of the dominant turbulence frequency to lower frequencies than in the incoming flow. Furthermore, the massflux spectra inside the separation bubble contain significant energy at the low frequencies of the shock motion. Our simulation shows a strong statistical link between the shock motion and the fluctuations in the separated, downstream flow, in the range of low frequencies that are characteristic of the shock motion.

Acknowledgments

This work is supported by the Air Force Office of Scientific Research under grant AF/9550-09-1-0464.

References

[1]Wu, M. and Martin, M. P., "Direct Numerical Simulation of Supersonic Turbulent Boundary Layer over a Compression Ramp," *AIAA Journal*, Vol. 45, No. 4, 2007, pp. 879–889.

[2]Smits, A. J. and Dussauge, J. P., *Turbulent Shear Layers in Supersonic Flow*, Springer Verlag, New York, 2nd ed., 2006.

[3]Erengil, M. E. and Dolling, D. S., "Correlation of Separation Shock Motion with Pressure Fluctuations in the Incoming Boundary Layer," *AIAA Journal*, Vol. 29, No. 11, 1991, pp. 1868–1877.

[4]Wu, P. P. and Miles, R. B., "Megahertz Visualization of Compression-Corner Shock Structures," *AIAA Journal*, Vol. 39, No. 8, 2001, pp. 1542–1546.

[5]Wu, M. and Martin, M. P., "Analysis of Shock Motion in Shockwave and Turbulent Boundary Layer Interaction using Direct Numerical Simulation Data," *Journal of Fluid Mechanics*, Vol. 594, 2008, pp. 71–83.

[6]Ganapathisubramani, B., Clemens, N. T., and Dolling, D. S., "Effects of upstream boundary layer on the unsteadiness of shock-induced separation," *Journal of Fluid Mechanics*, Vol. 585, 2007, pp. 369–394.

[7]Pirozzoli, S. and Grasso, F., "Direct Numerical Simulation of Impinging Shock Wave/Turbulent Boundary Layer Interaction at M=2.25," *Physics of Fluids*, Vol. 18, No. 065113, 2006.

[8]Dupont, P., C., H., and Debiève, J. F., "Space and time organization in a shock-induced separated boundary layer," *Journal of Fluid Mechanics*, Vol. 559, 2006, pp. 255–277.

[9]Dussauge, J. P., Dupont, P., and Debiève, J. F., "Unsteadiness in Shock Wave Boundary Layer Interactions with Separation," *Aerospace Science and Technology*, Vol. 10, No. 2, 2006.

[10]Bookey, P. B., Wyckham, C., Smits, A. J., and Martin, M. P., "New Experimental Data of STBLI at DNS/LES Accessible Reynolds Numbers," *AIAA Paper No. 2005-309*, Jan. 2005.

[11]Bookey, P. B., Wyckham, C., and Smits, A. J., "Experimental Investigations of Mach 3 Shock-Wave Turbulent Boundary Layer Interactions," *AIAA Paper No. 2005-4899*, June 2005.

[12]Ringuette, M. J., Wu, M., and Martin, M. P., "Low Reynolds Number Effects in a Mach 3 Shock Turbulent Boundary Layer Interaction," *AIAA Journal*, Vol. 46, No. 7, 2008.

[13]Ringuette, M. J. and Smits, A. J., "Wall-Pressure Measurements in a Mach 3 Shock-Wave and Turbulent Boundary Layer Interaction at a DNS-Accessible Reynolds Number," *AIAA Paper No. 2007-4113*, June 2007.

[14]Touber, E. and Sandham, N. D., "Oblique Shock Impinging on a Turbulent Boundary Layer: Low-Frequency Mechanisms," *AIAA Paper No. 2008-4170*, June 2008.

[15]Priebe, S., Wu, M., and Martin, M. P., "Direct Numerical Simulation of a Reflected-Shock-Wave/Turbulent-Boundary Layer Interaction," *AIAA Journal*, Vol. 47, No. 5, 2009, pp. 1173–1185.

[16]Martin, M. P., Taylor, E. M., Wu, M., and Weirs, V. G., "A Bandwidth-Optimized WENO Scheme for the Direct Numerical Simulation of Compressible Turbulence," *Journal of Computational Physics*, Vol. 220, 2006, pp. 270–289.

[17]Taylor, E. M., Wu, M., and Martin, M. P., "Optimization of Nonlinear Error Sources for Weighted Essentially Non-oscillatory Methods in Direct Numerical Simulations of Compressible Turbulence," *Journal of Computational Physics*, Vol. 223, 2006, pp. 384–397.

[18]Xu, S. and Martin, M. P., "Assessment of Inflow Boundary Conditions for Compressible Boundary Layers," *Physics of Fluids*, Vol. 16, No. 7, 2004, pp. 2623–2639.

[19]Martin, M. P., "Direct Numerical Simulation of Hypersonic Turbulent Boundary Layers. Part1. Initialization and Comparison with Experiments," *Journal of Fluid Mechanics*, Vol. 570, 2007, pp. 347–364.

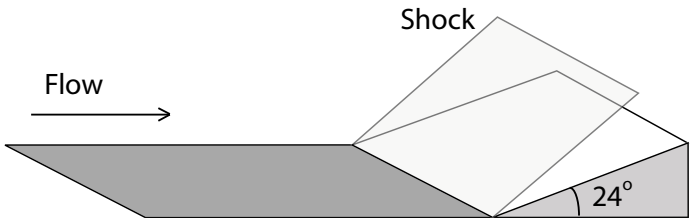

Figure 1. Inviscid flow schematic for the compression ramp configuration.

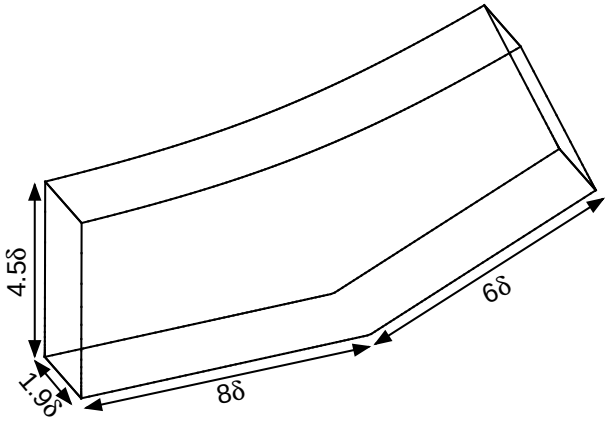

Figure 2. Computational domain for the DNS.

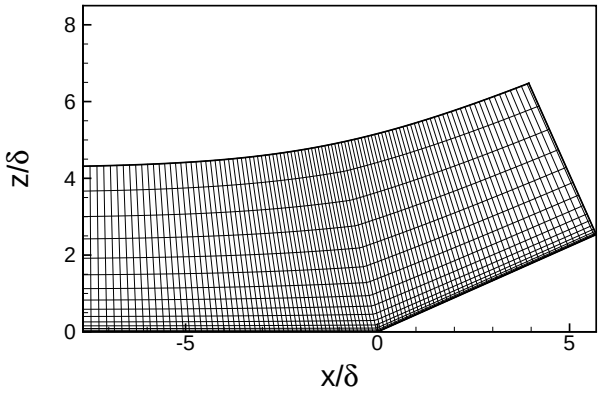

Figure 3. Sample grid for the DNS.

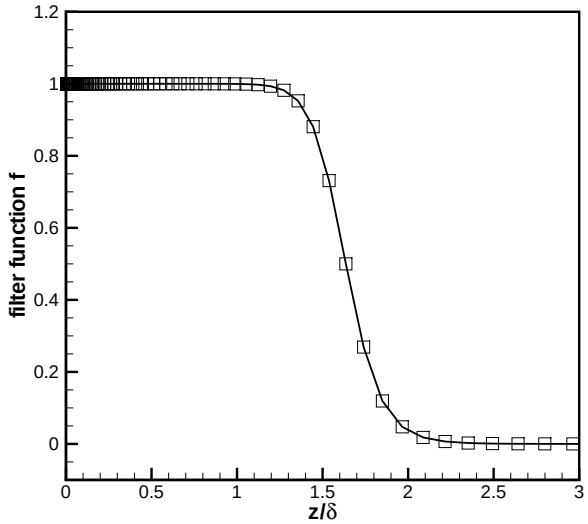

Figure 4. Filter function for the boundary layer DNS.

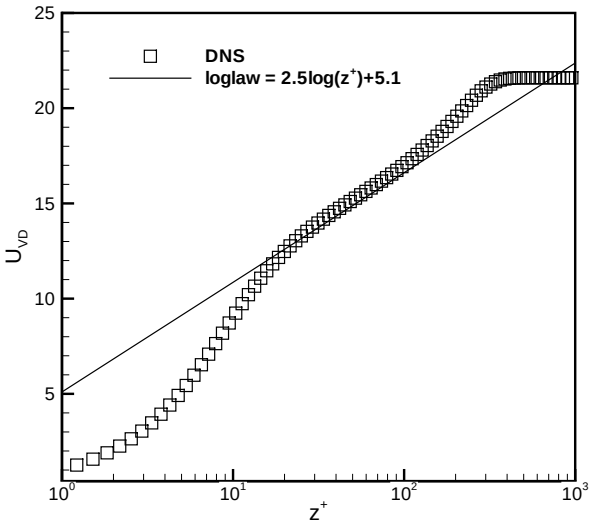

Figure 5. Van Driest-transformed velocity profile for the filtered boundary layer DNS.

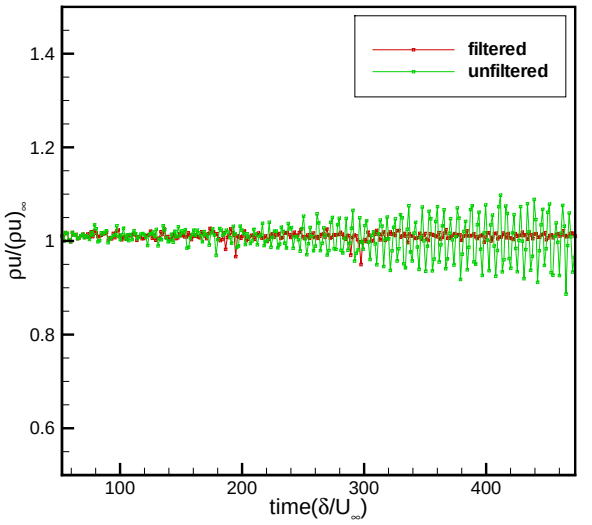

Figure 6. Spanwise-averaged mass-flux signal in the freestream ($z = 1.6\delta$) for the filtered boundary layer DNS.

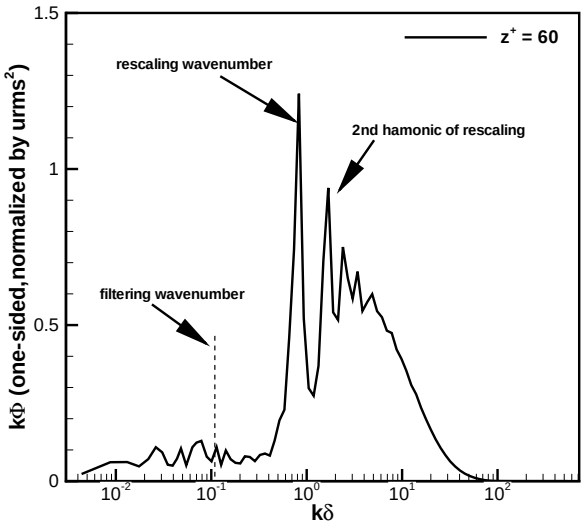

Figure 7. Streamwise velocity spectrum at $z^+ = 60$ (log layer) in the filtered boundary layer DNS.

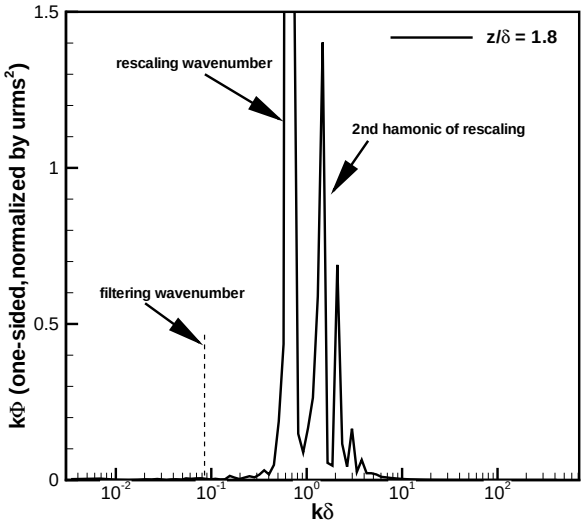

Figure 8. Streamwise velocity spectrum at $z = 1.8\delta$ in the filtered boundary layer DNS.

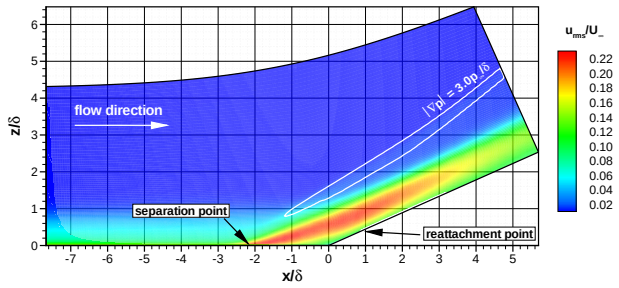

(a)

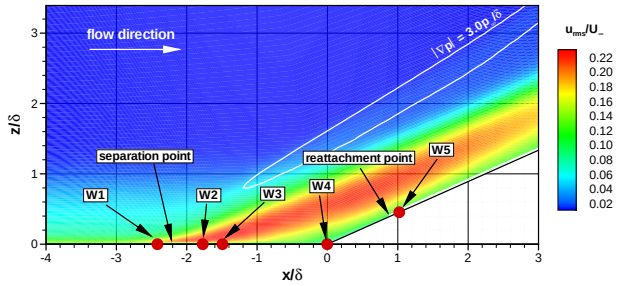

(b)

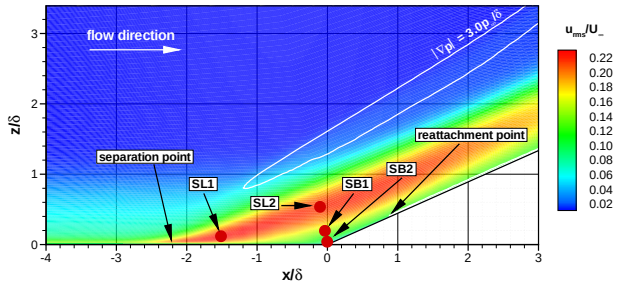

(c)

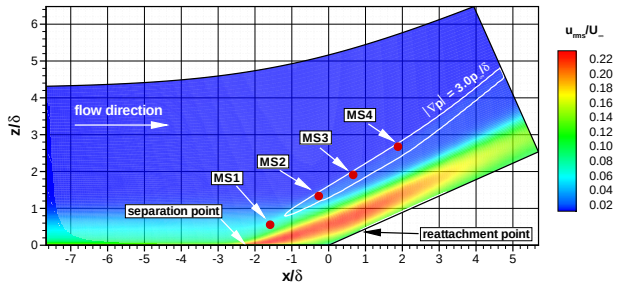

(d)

Figure 9. Contours of u_{rms} (flood) and $|\nabla p|$ (line) for the DNS. (a) General organization of the flow. (b) Detail of (a), showing the location of sampling points along the wall. (c) Location of sampling points in the separated shear layer and inside the separation bubble. (d) Location of sampling points at the mean shock location (determined from a pressure threshold criterion, see text) at different distances above the wall.

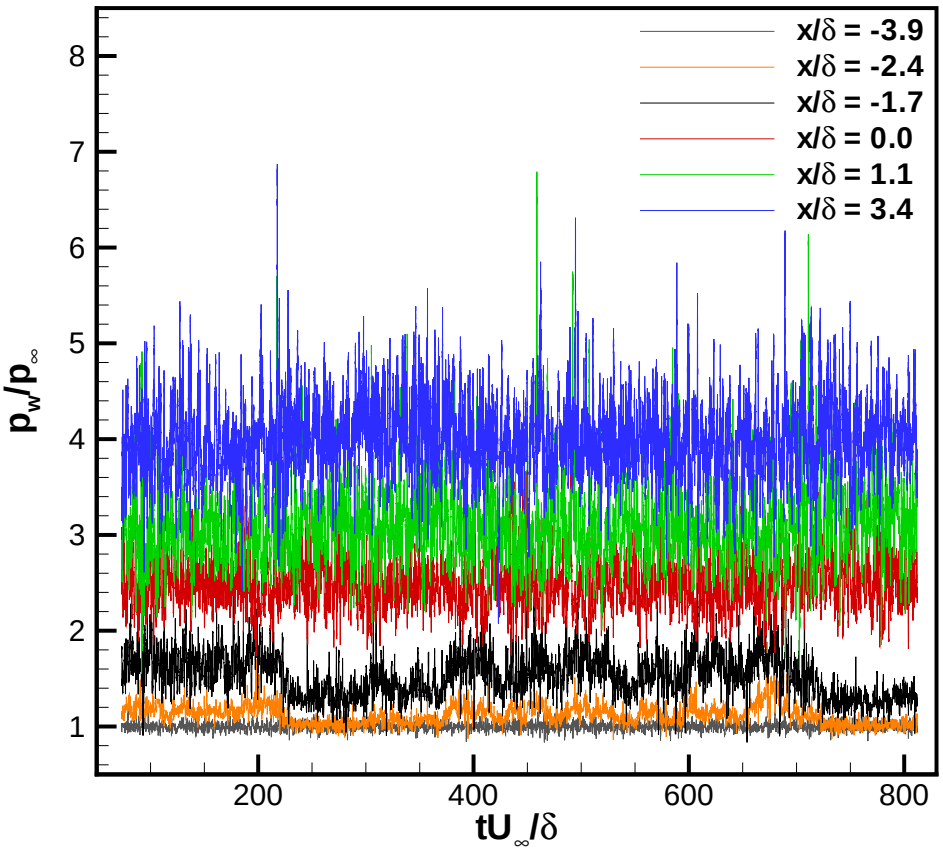

Figure 10. Wall-pressure signals at different streamwise locations for the DNS.

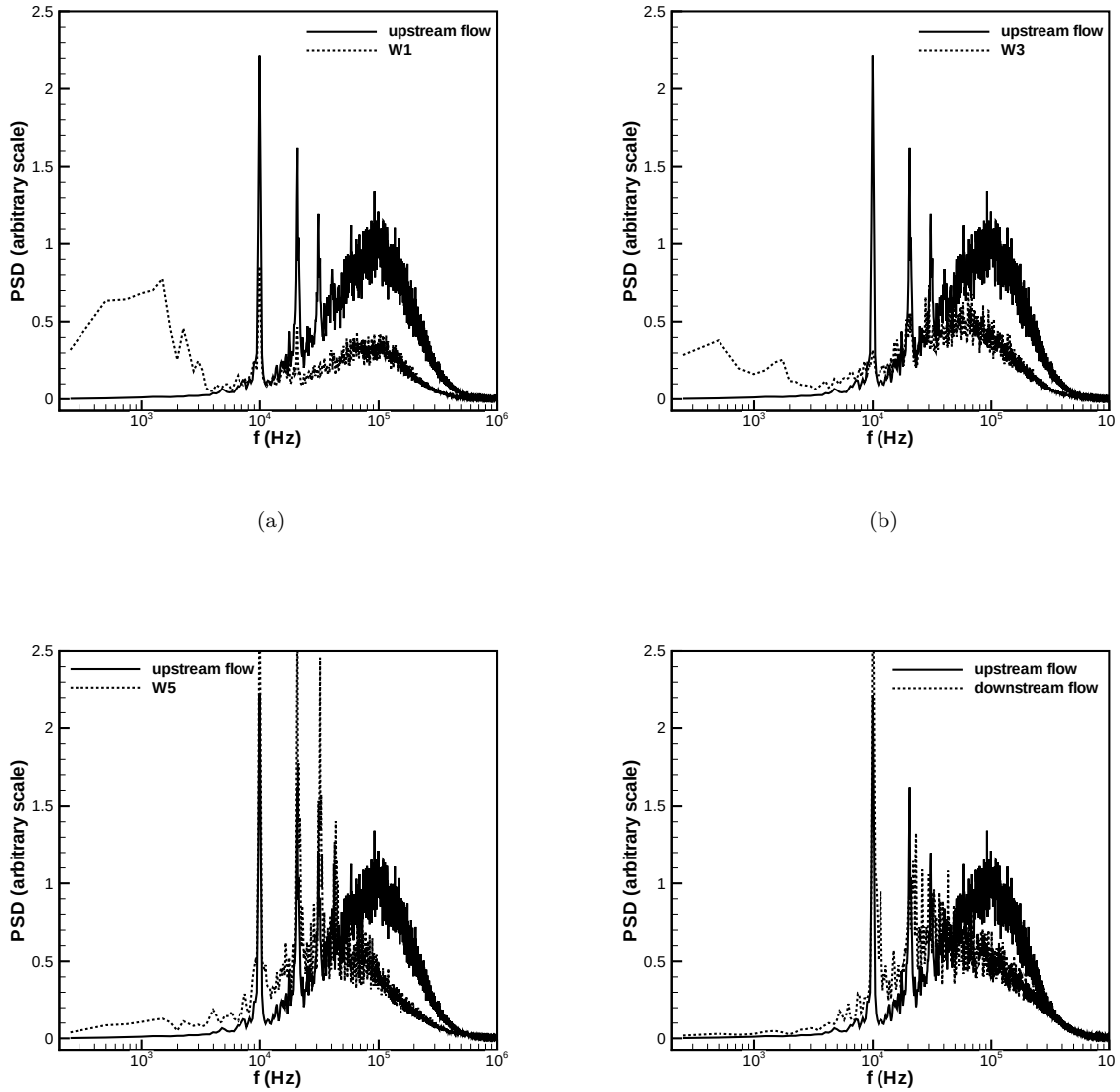

(a) (b)

(c) (d)

Figure 11. PSD of wall-pressure signals at different streamwise locations for the DNS.

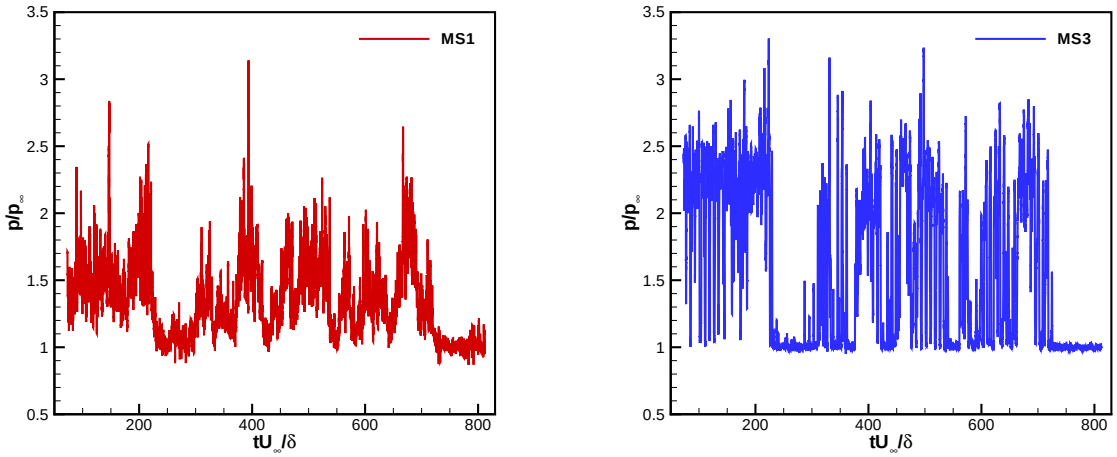

(a) (b)

Figure 12. Pressure signals taken at the mean shock location at (a) $z = 0.6\delta$ (location MS1) and (b) $z = 1.9\delta$ (location MS3).

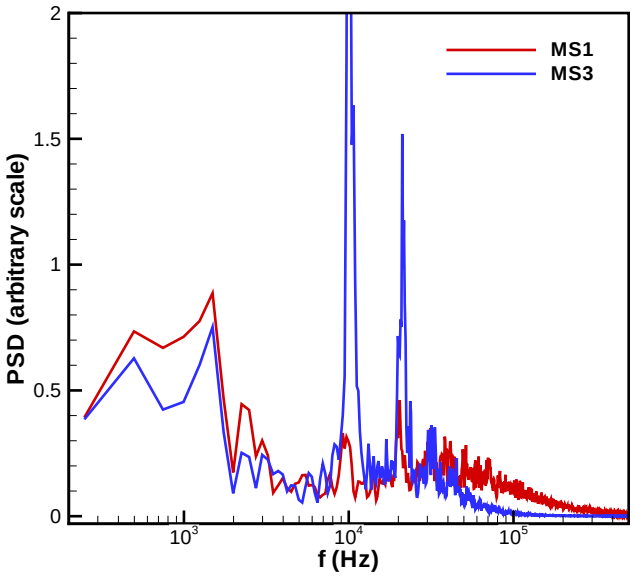

Figure 13. Power spectra of the pressure signals taken at the mean shock location at two different heights above the wall.

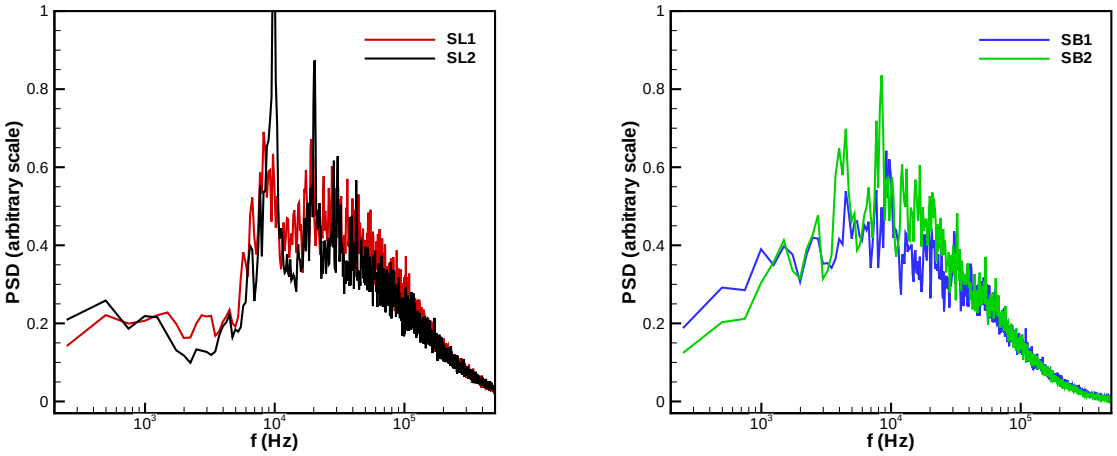

(a) (b)

Figure 14. Spectra of streamwise massflux fluctuations in (a) the separated shear layer and (b) the separation bubble.

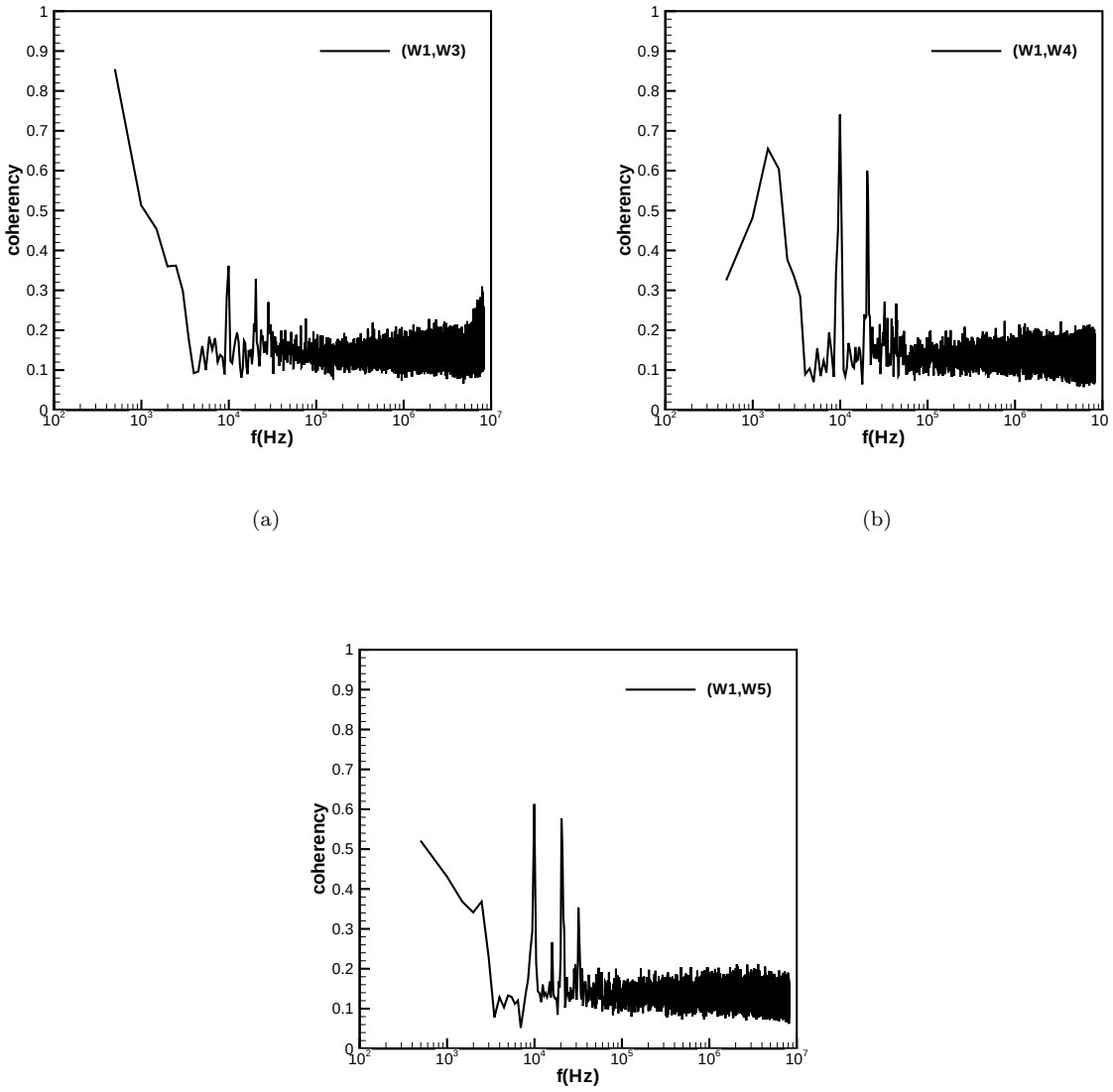

Figure 15. Magnitude-squared coherency function between the wall-pressure signal near the mean-flow separation point (W1) and different points under the separation bubble up to the mean-flow reattachment point.

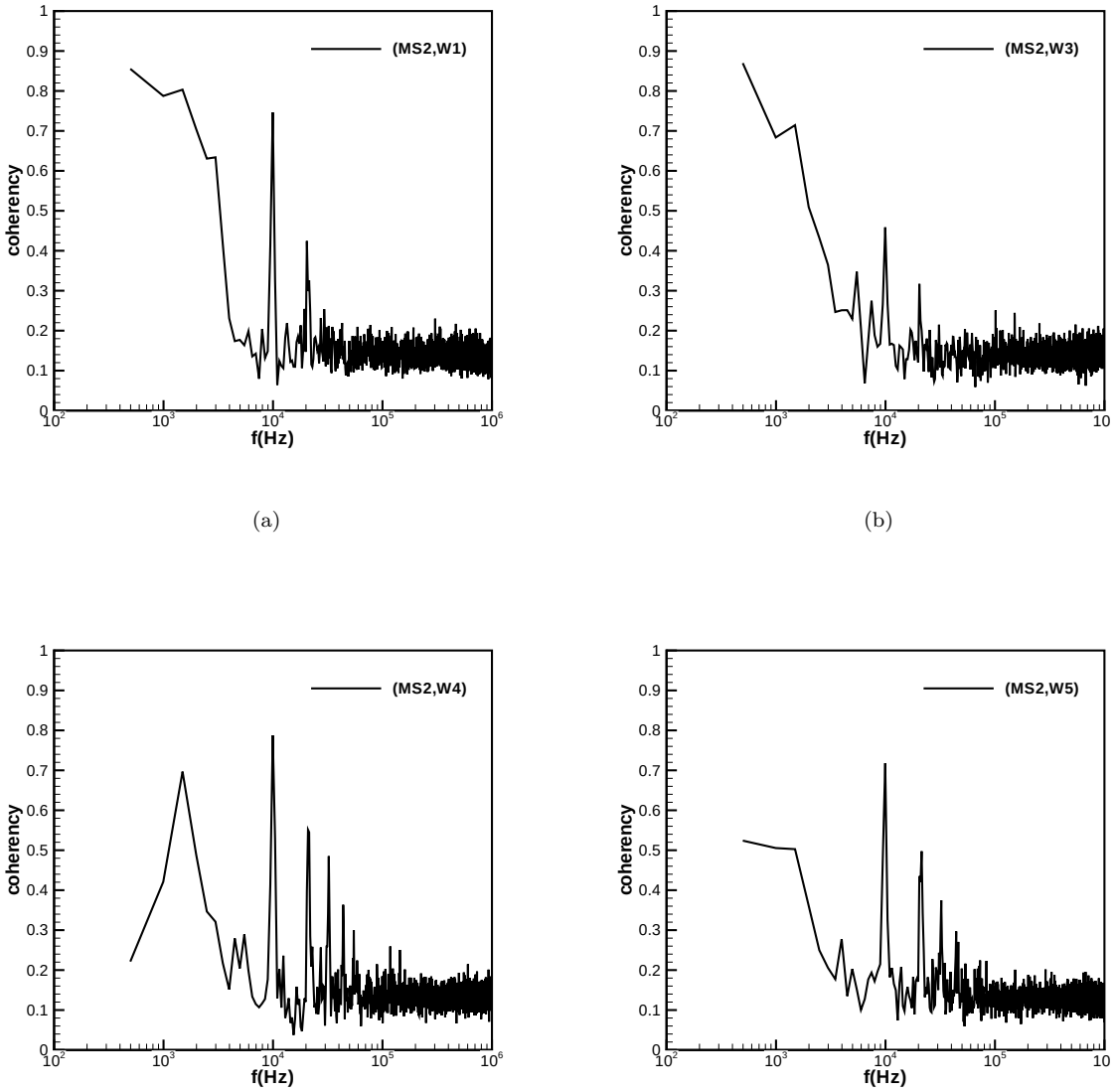

Figure 16. Magnitude-squared coherency between the pressure at the mean shock location at $z = 1.3\delta$ above the wall (MS2) and (a) the wall-pressure near the mean-flow separation point (W1), (b) the wall-pressure in the separated flow region (W3), (c) the wall-pressure at the corner (W4), and (d) the wall-pressure near the mean-flow reattachment point (W5).

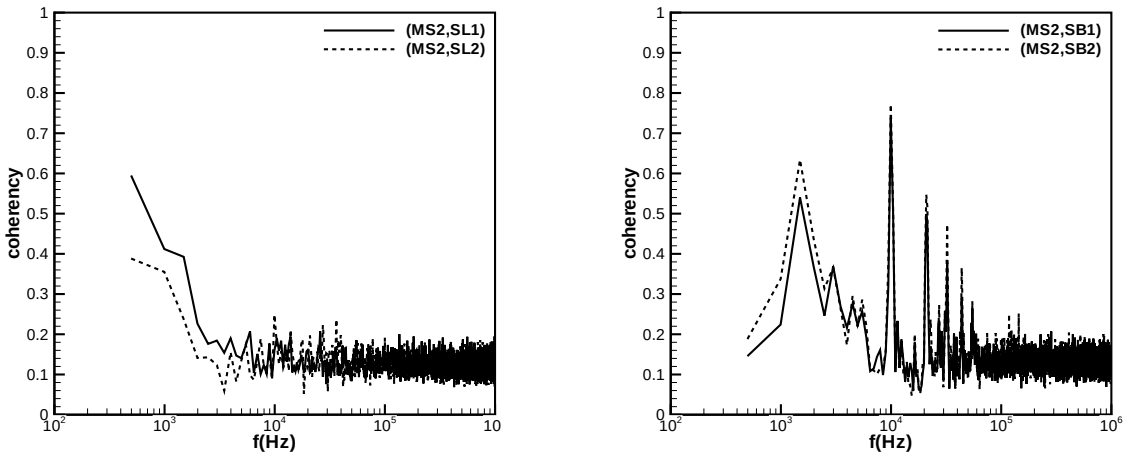

(a) (b)

Figure 17. Magnitude-squared coherency between the pressure at the mean shock location at $z = 1.3\delta$ above the wall (MS2) and (a) the massflux in the separated shear layer (SL1 and SL2), and (b) the massflux in the separation bubble (SB1 and SB2).